International Journal of Heat and Fluid Flow 32 (2011) 575–585

Contents lists available at ScienceDirect

International Journal of Heat and Fluid Flow

journal homepage: www.elsevier.com/locate/ijhff

A parametric study of adverse pressure gradient turbulent boundary layers

J.P. Monty *, Z. Harun, I. Marusic

Department of Mechanical Engineering, University of Melbourne, Victoria 3010, Australia

ARTICLE INFO

Article history:
Received 16 October 2010
Received in revised form 17 March 2011
Accepted 22 March 2011

Keywords:
Adverse pressure gradient
Boundary layer
Wall-turbulence

ABSTRACT

There are many open questions regarding the behaviour of turbulent boundary layers subjected to pressure gradients and this is confounded by the large parameter space that may affect these flows. While there have been many valuable investigations conducted within this parameter space, there are still insufficient data to attempt to reduce this parameter space. Here, we consider a parametric study of adverse pressure gradient turbulent boundary layers where we restrict our attention to the pressure gradient parameter, β, the Reynolds number and the acceleration parameter, K. The statistics analyzed are limited to the streamwise fluctuating velocity. The data show that the mean velocity profile in strong pressure gradient boundary layers does not conform to the classical logarithmic law. Moreover, there appears to be no measurable logarithmic region in these cases. It is also found that the large-scale motions scaling with outer variables are energised by the pressure gradient. These increasingly strong large-scale motions are found to be the dominant contributor to the increase in turbulence intensity (scaled with friction velocity) with increasing pressure gradient across the boundary layer.

1. Introduction

Turbulent boundary layers developing in the presence of a pressure gradient occur in all bluff-body flows (the trailing edge of an airfoil is a well-known example) and in diffuser flows. As such, the understanding of adverse pressure gradient (APG) boundary layers is of critical importance to a wide range of engineering applications. Furthermore, the phenomena of boundary layer separation occurs when the flow encounters an adverse pressure gradient. For these reasons APG boundary layers have been the subject of numerous experimental and numerical investigations since the mid-twentieth century. Table 1 lists some of the parameters for a selection of the existing database. While each of these studies has revealed important characteristics of pressure gradient flows, they collectively expand the parameter space that is known to affect the boundary layer. A significant barrier to progress in understanding the effects of pressure gradients on boundary layers is the uncertainty over the importance of each of the parameters. As a result, there has been little progress in reducing the parameter space for the purposes of prediction and control.

While there are many open questions regarding APG turbulent boundary layers, there are some established behaviours that should be summarised here. The most recognisable feature of an APG flow is the amplified wake of the mean velocity profile. Samuel and Joubert (1974), Nagano et al. (1998) and Aubertine and Eaton (2005) among others, have shown that the wake strength increases with the pressure gradient. Perry et al. (2002) and others have provided relationships between the pressure gradient parameter β and the wake strength for equilibrium boundary layers; these are always increasing, monotonic functions. Traditionally, the evolution of the boundary layer has been characterised by the shape factor, H, of the mean velocity profile. This parameter has been shown to increase in the presence of an adverse pressure gradient (see, for example, Nagano et al., 1998; Spalart and Watmuff, 1993; Skåre and Krogstad, 1994). The turbulence intensity in the outer region has also been found to rise with pressure gradient as shown by Marusic and Perry (1995) when scaled with the friction velocity (in addition to all previous references). More recently, Nagano et al. (1998) observed that the mean velocity profile in the logarithmic region was shifted below the classical log law in APG boundary layers. Spalart and Watmuff (1993) found a similar result, however they also noted that the apparent value of κ decreased with pressure gradient.

Although these characteristics are known, the role of the various candidate parameters is uncertain. Therefore, the aim of this study is to independently investigate the effects of three parameters that are known to be influential in adverse pressure gradient turbulent boundary layers:

1. *Pressure gradient parameter*

$$\beta = \frac{\delta^*}{\tau_o}\frac{\mathrm{d}P}{\mathrm{d}x},$$

* Corresponding author.
E-mail address: montyjp@unimelb.edu.au (J.P. Monty).

0142-727X/$ - see front matter Crown Copyright © 2011 Published by Elsevier Inc. All rights reserved.
doi:10.1016/j.ijheatfluidflow.2011.03.004

Table 1
Flow and experimental parameters for existing adverse pressure gradient boundary layer data. z^+_{min} is the minimum non-dimensional wall-distance measureable with the instrumentation available. Other parameters are defined in the text.

Authors	l^+	z^+_{min}	β	Re_θ
Samuel and Joubert (1974)	24–65	12	0.09–8	5000–30000
Cutler and Johnston (1989)	60–70	12	2–12	12000–25000
Nagano et al. (1998)	7.9–15.6	1	0.76–4.66	1290–3350
Skåre and Krogstad (1994)	≈11	3	12–21	25000–54000
Marusic and Perry (1995)	7–38	20	0–7	2200–19100
Aubertine and Eaton (2005)	3–4	3	−0.4–2.3	3000–6300
Skote et al. (1998)	DNS	DNS	0.24–0.65	360–690
Lee and Sung (2008)	DNS	DNS	0.25–1.68	850–1400

where δ^* is the displacement thickness, P the static pressure, x the streamwise coordinate and τ_o the wall shear stress. This parameter was proposed by Clauser (1954) who wrote that it represents the ratio of the pressure gradient force ($\delta^* \mathrm{d}P/\mathrm{d}x$) to "the only other gross force on the layer", the wall friction, τ_o. This is the most commonly discussed of the parameters affecting pressure gradient boundary layers. One reason for this is that β being constant is a necessary condition of an "equilibrium" boundary layer. Here, we adopt the simplified definition of equilibrium, which relates only to the similarity of the mean velocity deficit profile (Marusic et al., 2010c).

2. *Friction Reynolds number*

$$Re_\tau = \frac{\delta U_\tau}{\nu},$$

where δ is the boundary layer thickness, $U_\tau = \sqrt{\tau_o/\rho}$ is the friction velocity, ρ is the density and ν is the kinematic viscosity of the working fluid. This parameter may be thought of as a ratio of large-scale to small-scale motions in wall-turbulence and is the sole parameter for zero pressure gradient flows (since there is a monotonic relationship between this and the Reynolds number based on momentum or displacement thickness). The recent study by Hutchins et al. (2009) has shown that the turbulence intensity of ZPG boundary layers increases throughout the layer with Reynolds number. As mentioned above, increasing APG strength also has this effect. Therefore, it is necessary to isolate these two parameters in order to understand the contributions from each.

3. *Acceleration parameter*

$$K = \frac{\nu}{U_1^2}\frac{\mathrm{d}U_1}{dx},$$

where U_1 is the local free-stream velocity. This parameter uniquely characterises equilibrium boundary layers since β is constant in those flows. For the developing APG boundary layer, the importance of K is not clear from analysis of the existing literature.

Other parameters also exist as discussed by Perry et al. (2002), with the classical one being the Coles (1956) wake factor. However, this parameter is based on the premise that a universal logarithmic law of the wall exists.

2. Experimental procedure

2.1. Flow facility

The experiments were performed in an open-return blower wind tunnel. The important features of the tunnel are a settling chamber containing honeycomb and five screens followed by a contraction with an area ratio of 8.9:1, which leads into an initial inlet section area of 940 × 375 mm. For this investigation a new, flexible test section ceiling was made from acrylic and hung by threaded rods such that its height is easily adjusted; the adjustable section length is 4.2 m. For all data presented here, the sections heights are 375 mm at the trip wire (x = 0 m), 400 mm at x = 3 m, and 550 mm at x = 5 m. At no location is the boundary layer thickness greater than 20% of the tunnel height, ensuring the boundary layers on the floor and ceiling of the tunnel do not influence each other. The geometry is shown in Fig. 1. This facility was previously used by Marusic and Perry (1995) and Jones et al. (2001) and further details can be found in these references. To maintain a constant pressure gradient, the cross-sectional area of the tunnel increases nominally exponentially.

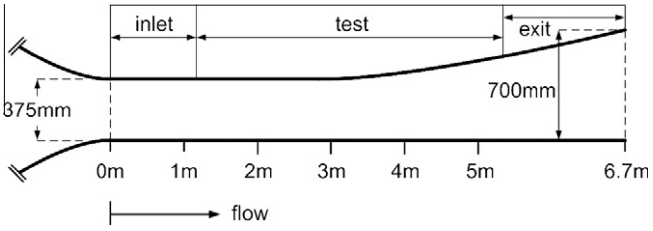

Fig. 1. Illustration of the wind-tunnel geometry (side view).

2.2. Oil-film interferometry

The method of oil-film interferometry (OFI) was used independently to determine the skin-friction coefficient C_f. Thirty cSt *Dow Corning* 200 silicone oil was dropped onto a glass plug inserted in the wind-tunnel floor at each location where velocity profiles were acquired. After placing the oil droplet, the air flow was increased from zero velocity to the measurement velocity in no more than 60 s. Temperature and pressure were sampled while real-time images of fringes of the droplet were taken using a Nikon D90 digital camera with a 105 mm lens. *OSRAM Vialox SON-E* 70 or 90 watt high-pressure sodium lamps were used to generate the fringe patterns. The fringe pattern results from the interference between the light reflected from the wind-tunnel (glass) floor and the inclined oil-air interface. The rate of change of the distance between fringes is related to the local shear stress,

$$\tau_o = \mu_{oil}\left(\frac{\Delta x}{\Delta t}\right)\frac{2\sqrt{n_{oil}^2 - n_{air}^2 sin^2\theta}}{\lambda}, \quad (1)$$

where θ is the illumination incident angle, n_{air} and n_{oil} are refractive indices of air and oil and λ is the wavelength of the light source (λ = 589.9 nm for the sodium lamp used). Further details of the

Table 2
Experimental parameters for hot-wire experiments. All data from the University of Melbourne.

Symbols	U_1 m/s	x m	δ m	Re_τ	Re_{δ^*}	Re_θ	β	$K\times10^{-7}$	ν/U_τ μm	d μm	l^+	t^+	TU_1/δ
▽[a]	11.97	5.0	0.098	2820	14,860	10,050	ZPG	ZPG	35.0	3.8	22	0.53	14,600
♦[b]	17.53	4.6	0.078	2860	17,540	11,860	1.90	−1.44	29.1	3.8	24	0.42	27,000
▷[c]	14.24	3.0	0.052	1820	6900	5020	ZPG	ZPG	28.7	2.5	17	0.38	21,800
◇[c]	12.70	3.5	0.061	1860	8560	6090	0.82	−1.44	32.4	2.5	15	0.28	31,000
o[c]	11.40	4.1	0.078	1940	10,070	6860	1.77	−1.96	40.7	2.5	16	0.19	21,900
□[c]	10.07	4.6	0.093	1980	12,730	8310	3.12	−2.56	47.2	2.5	16	0.14	18,400
∗[c]	9.80	4.8	0.104	1980	15,200	9440	4.74	−2.82	53.0	2.5	15	0.11	22,500
⊞[d]	7.98	4.8	0.108	1770	12,290	7620	4.39	−3.47	62.1	2.5	15	0.08	18,000
⊠[d]	12.89	4.8	0.100	2500	18,410	11,640	4.40	−2.18	40.8	2.5	16	0.19	16,000
⊡[d]	17.10	4.8	0.105	3510	25,100	16,260	4.53	−1.59	30.3	2.5	16	0.34	19,600
⊛[d]	19.06	4.8	0.102	3880	28,440	18,500	4.40	−1.46	27.5	2.5	16	0.41	19,300
+[e]	12.19	3.5	0.063	1910	8500	6050	0.96	−1.52	34.5	2.5	15	0.26	29,000
×[e]	14.38	4.1	0.073	2500	12,900	8860	1.67	−1.53	31.0	2.5	17	0.28	23,900
◁[e]	16.41	4.6	0.093	3280	21,310	14,080	3.22	−1.51	29.0	2.5	16	0.30	26,600
★[e]	18.02	4.8	0.105	3630	26,460	17,070	4.75	−1.52	29.4	2.5	16	0.31	26,500

[a] ZPG data (Hutchins et al., 2009).
[b] Matched ZPG data.
[c] Matched Re_τ data.
[d] Matched β data.
[e] Matched K data.

OFI method can be found in Ng et al. (2007), Madad et al. (2010). Determining fringe spacing can be problematic if image quality is compromised. To reduce error in the image analysis, the Hilbert Transform method discussed by Chauhan et al. (2010) is employed.

2.3. Experimental parameters

All of the measurements were performed using single hot-wire anemometry. Wollaston wires were soldered to the *DANTEC* prong tips and etched to give a platinum filament of the desired length, l. For the parametric study, the platinum filament diameter was ϕ = 2.5 μm, however, in Section 4, a diameter of ϕ = 3.8 μm was used to match experimental conditions of comparative studies. The hot-wire probes were operated in constant temperature mode using an *AA Lab Systems AN-1003* anemometer with an overheat ratio of 1.8 and the system had a frequency response of at least 50 kHz.

Previous investigations have shown that the length-to-diameter ratio (l/d) of hot-wire sensors should exceed 200 in order to minimize attenuation caused by end conduction effects (Ligrani and Bradshaw, 1987; Hutchins et al., 2009). This criteria has been followed in all the experiments in this study. Furthermore, these previous studies have also shown that the dimensionless wire length l^+ should be as small as possible to reduce spatial resolution effects. Unfortunately, it is not practical to reduce the wire size sufficiently to capture the smallest structures encountered in the boundary layers of this study. However, when comparing data, Hutchins et al. (2009) have shown that it can be useful to match l^+ between experiments in order to maintain a similar attenuation across all data sets. For the parametric study here $l^+ = 16 \pm 1$, and in experiments conducted for comparison with published zero pressure gradient data, l^+ was matched with the published data.

The sampling time at each wall-normal location, T, is non-dimensionalised in outer-scaling to give 'boundary layer turnover' times, TU_1/δ. It is important to consider this parameter when selecting the sampling time for an experiment since the largest flow features can exceed 6δ in wavelength (Hutchins and Marusic, 2007; Monty et al., 2007; Ganapathisubramani et al., 2003) and converged statistics typically require several thousand of these events to advect past the sensor. For this reason, the boundary layer turnover time was at least 15,000 in the experiments performed during this investigation.

All relevant experimental parameters are provided in Table 2. Note that the superscript '+' is used to denote viscous scaling, e.g. $z^+ = zU_\tau/\nu$, $U^+ = U/U_\tau$, $t^+ = tU_\tau^2/\nu$. U_τ is the friction velocity and $t^+ = tU_\tau^2/\nu$ is the non-dimensionalised sample interval, where $t = 1/f_s$ and f_s is sampling rate. z is the wall-normal coordinate.

3. Flow conditions

3.1. Pressure gradient

The wind-tunnel is constructed in three sections: an inlet section with fixed-height ceiling, a variable pressure gradient section and an exit section (as shown in Fig. 1). The variable pressure gradient section has an adjustable, flexible ceiling that is configured such that a zero pressure gradient is maintained until $x \approx 3$ m. A constant adverse pressure gradient is thereafter maintained until $x \approx 5$ m. After final adjustments to the ceiling height were made, it was found that the coefficient of pressure, C_p

$$C_p = \frac{P - P_o}{\frac{1}{2}\rho U_0^2} = 1 - \left(\frac{U_1}{U_0}\right)^2 \tag{2}$$

remains within ±0.01 at a given streamwise location for the range of velocities tested. Here, P is the local static pressure, P_o is the static pressure at the inlet and U_0 is the inlet free-stream velocity. Fig. 2 shows C_p plotted against streamwise location for two selected inlet velocities.

3.2. Skin-friction

For the analysis of velocity statistics of wall-turbulence, it is necessary to be able to accurately measure the friction velocity, U_τ. This is commonly non-dimensionalised as the coefficient of friction

$$C_f = \frac{\tau_o}{\frac{1}{2}\rho U_1^2} = 2\frac{U_\tau^2}{U_1^2}, \tag{3}$$

where τ_o is the wall shear stress, which is measured using the oil-film interferometry method described earlier. It is important to note that there is a difference between U_τ measured with OFI and that determined by the Clauser method using the mean velocity profile. To illustrate this point, Fig. 3 displays the coefficient of friction plotted as a function of pressure gradient parameter, β (Reynolds number is maintained constant). The skin friction determined from the

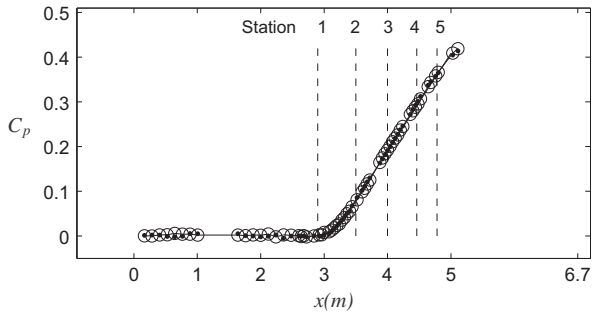

Fig. 2. Coefficient of pressure C_p. ○, $U_0 = 15.9$ m/s and •, $U_0 = 10.5$ m/s.

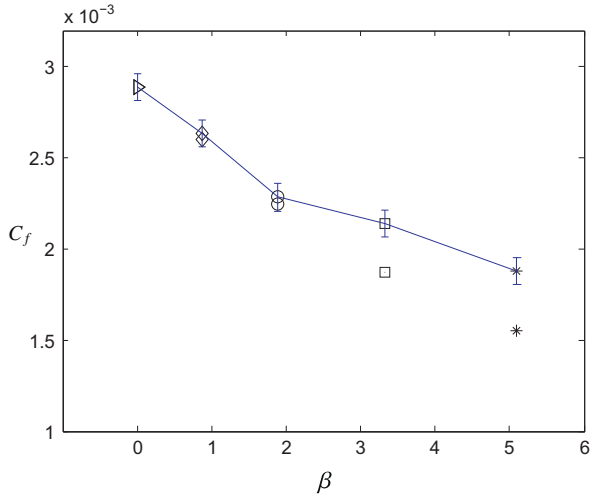

Fig. 3. Coefficient of friction for constant $Re_\tau \approx 1900$. The solid line connects C_f obtained directly by OFI. The error bars of 2.5% for the OFI method are shown. Symbols not connected with the solid line represent C_f obtained from Clauser chart. Refer to Table 2 for symbols.

Clauser chart method agrees with that obtained from oil-film interferometry *only* for zero and mild adverse pressure gradient boundary layer flows. Beyond $\beta \approx 2$, the difference between the methods becomes significant (approximately 10% difference in C_f). This suggests that the use of the Clauser chart for moderate to strong adverse pressure gradients could lead to inaccurate conclusions about the applicability of scaling arguments for pressure gradient boundary layers.

Throughout this paper U_τ is determined by oil-film interferometry (except in the case of the zero pressure gradient data of Hutchins et al., 2009, where the Clauser method was used).

4. Comparison of APG and ZPG flows at $Re_\tau = 2800$

We begin our analysis by comparing one relatively mild adverse pressure gradient case ($\beta = 1.90$) with a zero pressure gradient case published in Hutchins et al. (2009) at matched $Re_\tau \approx 2800$. By analysing only two data sets, this comparison is intended to provide clear and simple evidence of the effects of pressure gradient on the mean statistics.

4.1. Mean velocity

Fig. 4*a* displays the inner-scaled mean velocity profiles for both boundary layer flows. Although the Clauser method was used to determine U_τ by Hutchins et al. (2009), the brief analysis of the applicability of this method in Section 3.2 suggests that this should not affect any of the conclusions drawn here.

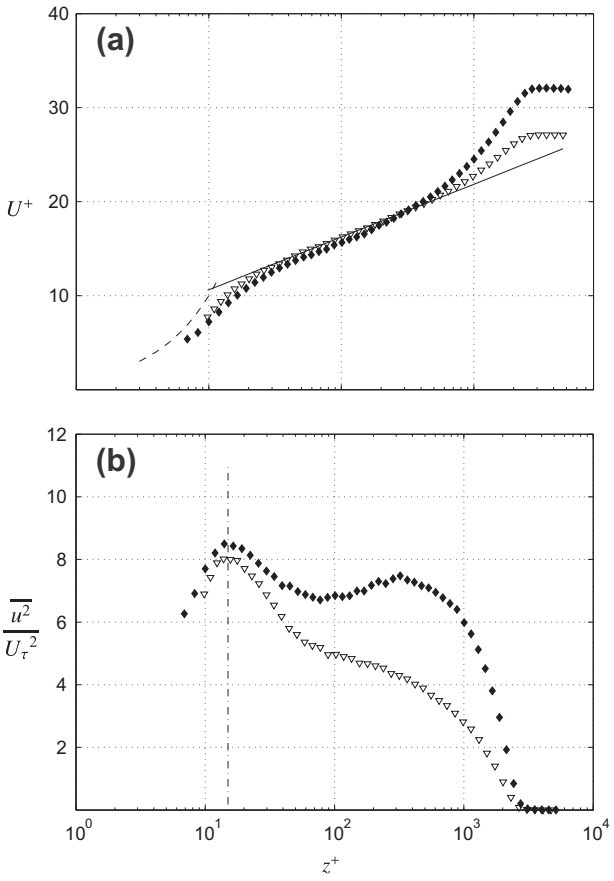

Fig. 4. Comparison of APG and ZPG flows at matched $Re_\tau \approx 2800$. (a) Mean velocity profiles and (b) broadband turbulence intensity profiles. (▽) ZPG and (♦) APG. Solid line shows Eq. (4) with $\kappa = 0.41$ and $A = 5.0$, dashed line shows $U^+ = z^+$ and dashed-dot line $z^+ = 15$.

In the wake region ($z/\delta > 0.15$) the APG mean velocity rises higher than that of the ZPG case, typical of adverse pressure gradient boundary layers. The 'strength' of the wake is commonly quantified by the Coles wake parameter, Π (essentially a measure of the maximum deviation from the log law). Calculation of Π requires the explicit knowledge of the log law that describes the mean velocity data in the overlap region. That is, the constants κ and A in

$$U^+ = \frac{1}{\kappa}\log(z^+) + A, \tag{4}$$

must be known. The classical values for the smooth wall, zero pressure gradient boundary layer are $\kappa = 0.41$ and $A = 5.0$, which leads to a value of $\Pi \approx 0.55$ for the ZPG case. However, it is not trivial to determine Π for the APG case since an examination of the logarithmic region in Fig. 4*a* reveals that the APG mean velocity drops below the classical log law. This behaviour has been reported previously for strong pressure gradients (Nagano et al., 1998; Spalart and Watmuff, 1993; Lee and Sung, 2008), although it is noted that the measurements of Aubertine and Eaton (2005) in mild pressure gradient flows ($\beta < 2.3$) show the mean velocity does follow the classical log law within the considerable scatter of the data. The experiments of Aubertine and Eaton (2005) were conducted over an inclined 4° ramp; it is possible that flow development differences may be responsible for the different conclusions drawn from that work. Furthermore, by visual inspection of Fig. 4*a* it appears that

there is a difference in the extent of the logarithmic region for the two flows. The logarithmic layer is most commonly considered as the region of $100 < z^+ < 0.15Re_\tau$, however, there are numerous studies that challenge this (for example, Zagarola and Smits (1998), Österlund and Johansson (2000), Nagib and Chauhan (2008), Bourassa and Thomas (2009)). For the ZPG case presented here, the logarithmic region appears to begin at $z^+ \approx 70$ and extends until $z^+ \approx 0.15Re_\tau$, which is slightly more extensive than generally accepted. Although it is not so clear in the APG case, it appears that the mean velocity profile deviates closer to the wall than in ZPG (it is interesting to note that in the favorable pressure gradient case, Bourassa and Thomas (2009) found the log region to be longer compared with the ZPG case).

To more accurately evaluate the extent of the overlap region and the logarithmic scaling of the mean velocity, it is helpful to employ the diagnostic function

$$\Xi = z^+ \frac{dU^+}{dz^+}. \tag{5}$$

If there exists a logarithmic region of the velocity profile, it will appear in the range of z^+ for which Ξ is constant. In fact, it is easily shown by differentiating Eq. (4) that $\Xi = 1/\kappa$ in this region. A comparison of the diagnostic function for zero and adverse pressure gradients is shown in Fig. 5. The zero pressure gradient mean flow data seems to follow a logarithmic trend in the region $70 < z^+ < 0.15Re_\tau$. It is also evident that both cases agree well until $z^+ \approx 100$, from which point there is a deviation of the APG data. Although the diagnostic function data are noisy (inherent in the spatial differentiation of experimental data), it could be argued that the wake region of the APG flow begins as early as $z^+ = 150$ ($z/\delta = 0.05$). If so, there is effectively no logarithmic region at this pressure gradient and Reynolds number. However, *if* the traditional limits of $100 < z^+ < 0.15Re_\tau$ are employed, it is found that $\kappa = 0.32$ for the adverse pressure gradient case (with corresponding $A = 1.03$). This is in agreement with both Nagib and Chauhan (2008) and Nickels (2004) who also reported lower values of κ for APG compared with ZPG. Observing Fig. 5, it is obvious that the value of κ is strongly dependent on the chosen log region at this Reynolds number. For example, if we were to consider the region $70 < z^+ < 0.05Re_\tau$, the APG data follow a log law with $\kappa = 0.42$ and $A = 4.6$, while a curve-fit to the ZPG data gives $\kappa = 0.42$ and $A = 5.2$. It is not clear from the data presented here, or the existing literature, whether the limited extent of the log region in the APG case is due to the pressure gradient or the relatively low Reynolds number. Therefore, it is suggested that higher Reynolds number data are needed to make definite conclusions about the effect of pressure gradient on the log law using this analysis (as pointed out by Nagib and Chauhan, 2008). This also means that the wake parameter Π cannot be stated conclusively and could be in the range of $\Pi = 1.25 - 1.65$ depending on the log law chosen.

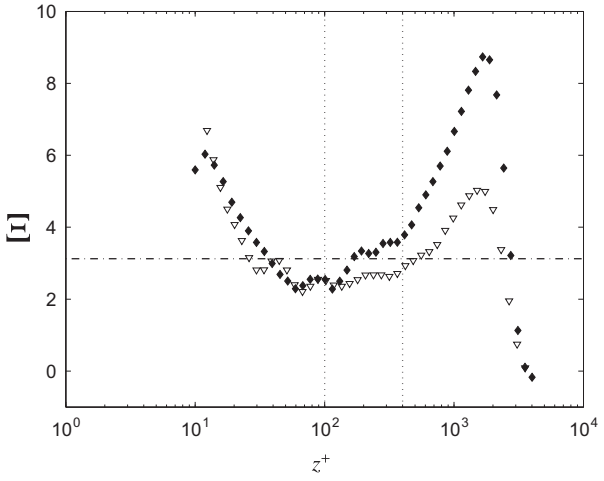

Fig. 5. Comparison of the diagnostic function for APG and ZPG flows at matched $Re_\tau \approx 2800$. For symbols, refer to Table 2. Dashed-dot line shows $\kappa = 0.32$, dashed lines show the logarithmic region.

4.2. Turbulence intensity

The scaling of the streamwise turbulence intensity near the wall in canonical turbulent shear flows remains an open question and has received increasing attention in the last decade (for example, Marusic et al., 2010c,, 2001; Smits et al., 2011; Hutchins et al., 2009; DeGraaff and Eaton, 2000). In the case of boundary layers subjected to pressure gradients, there is far less reliable data (covering the range of pressure gradients and Reynolds numbers) available to enable the formulation of scaling arguments for the second-order mean statistics. In Fig. 4*b*, turbulence intensity data from the APG and ZPG cases are presented. These data were acquired with carefully matched experimental conditions to permit a valid comparison between the two flows. Specifically, the Reynolds number (≈2800) and non-dimensional hot-wire length, l^+ (≈23) are matched.

For zero pressure gradient boundary layers, Hutchins et al. (2009) pointed out that the scatter in viscous-scaled turbulence intensity in the near-wall region is due in large part to the competing effects of Reynolds number and non-dimensionalised hot-wire length, l^+. That is, as Re_τ is increased, large-scale structures contribute to an increase in turbulence intensity, however as l^+ is increased, the small-scale fluctuations become increasingly attenuated, thus causing a decrease in measured turbulence intensity. For this reason, it is useful to match l^+ when comparing two data sets.

Fig. 4*b* displays broadband turbulence intensity scaled with U_τ for both the APG and ZPG cases. It is immediately clear that the turbulence intensity is higher throughout the flow for the APG case. The maximum difference occurs in the outer region where a secondary hump is observed in the APG data. No secondary hump is observed in the ZPG data at this Reynolds number as the turbulence intensity decays almost logarithmically through the

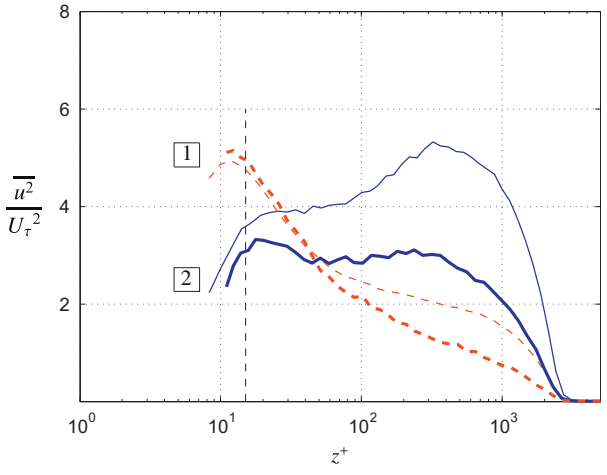

Fig. 6. Broadband turbulent intensity profiles for ZPG and APG data at $Re_\tau \approx 2800$ decomposed into a small-scale component ($\lambda_{xc} < \delta$, broken lines) and a large-scale component ($\lambda_{xc} > \delta$, solid lines). The heavier line represents the ZPG case, while the lighter represents the APG. The black dashed line indicates $z^+ = 15$. (For interpretation of the references to colour in this figure legend, the reader is referred to the web version of this article.)

logarithmic region. Clearly it will not be possible to collapse these profiles with a constant velocity scale. Scaling arguments alone are therefore unlikely to aid in the understanding of the differences in this statistic owing to pressure gradient. To identify the source of the differences observed in Fig. 4*b*, it is instructive to decompose the turbulence intensity into a large- and a small-scale component. This decomposition is similar to that proposed by Hutchins and Marusic (2007) and Mathis et al. (2009), who defined a cut-off wavelength based on an analysis of the pre-multiplied energy spectra map of the streamwise velocity component. Here a cut-off length-scale equal to the thickness of the boundary layer ($\lambda_{xc} = \delta$) was chosen. This cut-off length scale was used by Mathis et al. (2009) in the quantification of amplitude modulation of the small-scales of wall-turbulence in zero pressure gradient boundary layers. However, it is cautioned that this analysis requires high enough Reynolds number to ensure sufficient separation of scales; the data shown here are at the lower end of Reynolds numbers considered high enough for this purpose.

Fig. 6 shows the decomposed turbulence intensity profiles for ZPG and APG flows. It is observed that the large-scales are dominant in the outer region for both cases. However the large-scale energy contribution for the APG case is much higher throughout the flow, particularly in the outer region (where a secondary peak in the broadband turbulence intensity is present). Although there is also increased energy in the small-scales in the outer region of the APG boundary layer, it is the large-scale energy increase that is the greater contributor to the high turbulence intensity in this region. Furthermore, the large-scale component extends its presence from the outer and logarithmic regions down to the near-wall region. Interestingly, the adverse pressure gradient does not significantly change the small-scale component in the inner region ($z^+ \lesssim 50$). This might suggest that the near-wall cycle remains similar in both flows (analysis of other velocity components would be required to confirm this). Regardless, it is observed that the large-scale contribution near the wall is responsible for the difference in turbulence intensity in this region. The increased peak in broadband turbulence intensity (at $z^+ = 15$) for the APG case is therefore due to the increased 'footprint' of the large-scale features. Such an increased footprint was also reported by Hutchins and Marusic (2007) to explain the rise in peak turbulence intensity with Reynolds number for zero pressure gradient boundary layers.

5. A parametric study of Reynolds number and pressure gradient effects

As discussed in the introduction, there is a significant history of experimental research into boundary layers subjected to pressure gradients. However, there is limited knowledge of the effect of each of the relevant parameters in isolation. Here, the results of a dedicated study into the effects of pressure gradient parameter, β, Reynolds number, Re_τ, and acceleration parameter, K are presented. The reader may note that Table 1 is segregated into four groups of experimental results, of which the final three groups refer to the constant $Re_\tau \approx 1900$, constant $\beta \approx 4.4$ and constant $K \approx 1.5 \times 10^{-7}$ experiments respectively.

5.1. Constant Reynolds number

Fig. 7*a* shows the mean velocity profiles for adverse pressure gradient boundary layers with matched Reynolds number, $Re_\tau \approx 1900$, varying $\beta = 0$–4.7 and varying $K = 0$–2.8×10^{-7}. Each data set was acquired at a different streamwise location and it should be noted that a unique inlet free stream velocity is required to match Re_τ. In the outer region, the adverse pressure gradient causes the wake of the mean velocity profile to increase, as

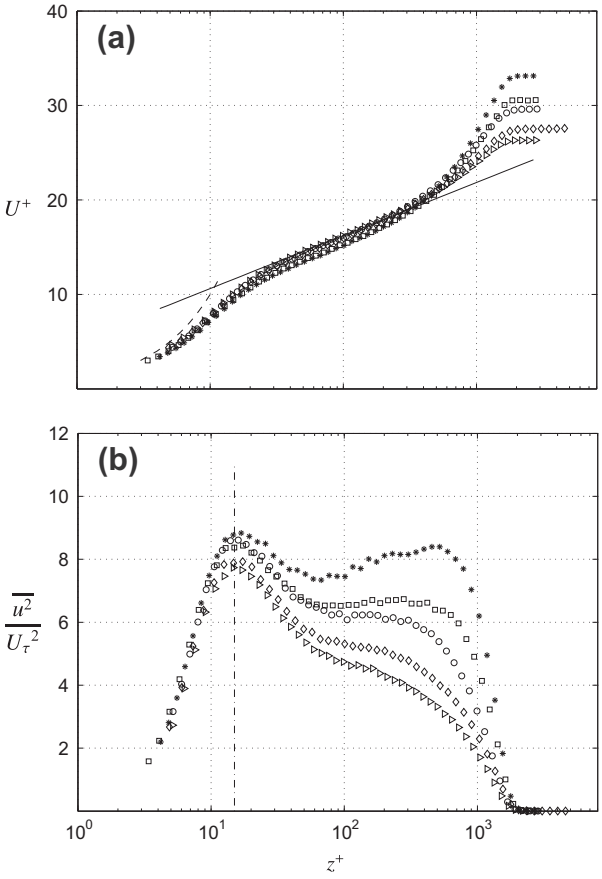

Fig. 7. Mean statistics for adverse pressure gradient boundary layers with $Re_\tau \approx 1900$. (a) Mean velocity and (b) turbulence intensity profiles. For symbols, refer to Table 2. The solid line shows Eq. (4) with $\kappa = 0.41$, $A = 5.0$, the dashed line shows $U^+ = z^+$ and the dashed-dot line indicates $z^+ = 15$.

expected. Focusing on the log region, there is a systematic deviation from the log law (downward) as pressure gradient is increased. Furthermore, the logarithmic region appears to reduce in size with increasing pressure gradient, consistent with the results of the previous section. Skåre and Krogstad (1994) proposed that the shift-down from the log law was due to the increased Reynolds number. In this experiment, the Reynolds number was maintained constant while the pressure gradient was increased, thus any Reynolds number effect was isolated so that the reduction in scaled mean velocity must be due to the pressure gradient.

In the near-wall region ($5 < z^+ < 15$), the mean velocity profiles are similar across all pressure gradients. This behaviour was also reported by Krogstad and Skåre (1995). It is also in agreement with Nickels (2004) who showed that, in the region of $z^+ < 10$, the mean velocity data of adverse, zero *and* favorable pressure gradients collapses under inner-scaling. (this conclusion was based on an analysis of the data in Nagano et al., 1998, and Spalart, 1986).

Fig. 7*b* shows the broadband turbulence intensity profiles for matched $Re_\tau \approx 1900$. It is reminded that the non-dimensionalised sensor length is maintained constant at l^+=16 ± 1 for all experiments to ensure similar spatial resolution effects. As noted earlier, the effect of an adverse pressure gradient is to increase the turbulence intensity throughout the layer when scaled with U_τ. Fig. 7*b* shows just how the turbulence intensity profile grows with increasing pressure gradient. It is important to note that the trends observed and conclusions drawn from the scaled turbulence intensity profiles will be considerably different if U_τ is obtained by the Clauser method. For the inner region, the peak value of turbulence intensity rises weakly from ~7.8–9. In the outer region, however,

the turbulence intensity increases sharply as pressure gradient increases. Because the intensity in the outer region rises faster than the inner, at $\beta = 4.7$ (the strongest pressure gradient) the intensity in the outer region almost reaches the near-wall peak value. This leads to the 'double-hump' shape of the turbulence intensity profile and a further increase in β would undoubtedly lead to a primary peak in the outer region. Clearly, then, there is a notable change in the shape of the profile with β, which affirms that the adverse pressure gradient causes a change in the distribution of energy in a turbulent boundary layer. This change can be described as a relocation of the dominant energetic motions from the near-wall region to the outer region.

It was shown in Section 4.2 that a scale-based decomposition of the broadband turbulence intensity can provide insights into the relative contributions of small- and large-scales. Fig. 8 shows this decomposition for fixed Reynolds number with varying pressure gradient. The small-scale component is represented by the broken lines and is marked as group '1'. The large-scale component is represented by the solid lines and is marked as group '2'. The line thickness increases with pressure gradient strength.

As the pressure gradient increases, it appears that both the small- and large-scale contributions increase also. Even near the wall there is a weak increase in the small-scale turbulence intensity. However, as found in Section 4.2, it is the increasing large-scale component in the near-wall region which causes the peak turbulence intensity (at $z^+ = 15$) to rise with increasing adverse pressure gradient. In the outer region, the influence of the pressure gradient on the strength of the large-scale structures is clearly evident. These large-scales amplitude modulate the small-scales as discussed by Marusic et al. (2010b). For adverse pressure gradient flows, it is therefore suggested that the amplitude modulation will be stronger than the ZPG case, owing to the increased intensity of the large-scale structures. Overall there is an increased energy in all scales in the outer region when scaled with U_τ, which reaffirms the earlier suggestion that a bulk shift in energy occurs from the near-wall to the outer region as pressure gradient increases, concurrent with an amplification of the energy of the large-scale structures.

So far, scaling using the friction velocity U_τ has been used to characterise the effect of pressure gradient. Another scaling using the inlet velocity U_0 can also be used and this is shown in Fig. 9 for results at matched $Re_\tau \approx 1900$. We emphasise here again that

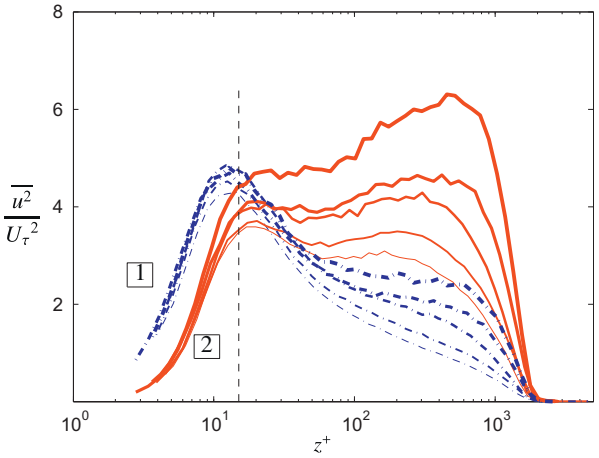

Fig. 8. Broadband turbulent intensity profiles for ZPG and APG data at $Re_\tau \approx 1900$ decomposed into a small-scale component ($\lambda_{xc} < \delta$, broken lines) and a large-scale component ($\lambda_{xc} > \delta$, solid lines). The thinnest line represents the ZPG case, the thickness of the line grows with the strength of APG. The black dashed line indicates $z^+ = 15$.

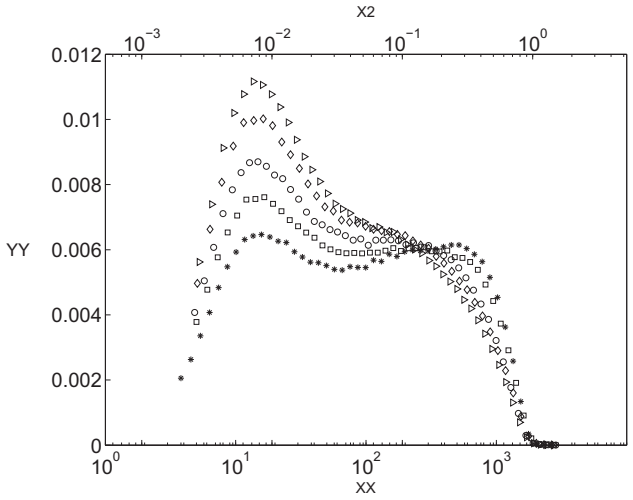

Fig. 9. Broadband turbulent intensity profiles for ZPG and APG data at $Re_\tau \approx 1900$ scaled with inlet velocity, U_0. For symbols, refer to Table 2.

in order to achieve a matched $Re_\tau \approx 1900$, U_0 had to be adjusted, thus there was a range of unique U_0 values for this case. Fig. 9 shows that the newly scaled turbulence intensity collapses in the outer region towards the edge of boundary layer ($z/\delta > 0.3$). Nearer to the wall, in contrast to the U_τ scaled data, this scaling suggests that turbulence intensities decrease with pressure gradient for $z^+ < 100$. The results in Fig. 9 highlight that the absolute values of the turbulence intensities tend to decrease with increasing pressure gradient in the inner region of the boundary layer, as found by Nagano et al. (1998). Throughout the remainder of this paper we consider only friction velocity scaling since the focus will be on identifying changes in the flow caused by pressure gradient relative to the zero pressure gradient case.

5.2. Constant pressure gradient parameter, β

We now isolate the pressure gradient parameter β to examine the effect of Reynolds number on an adverse pressure gradient boundary layer. Fig. 10*a* displays the mean velocity profiles for $\beta \approx 4.4$ with varying $Re_\tau = 1770$–3880. The mean velocity profiles collapse in the inner and logarithmic regions for all Reynolds numbers. These do not, however, collapse onto the classical log law (4), which is shown in the figure for comparison. Once again, it is difficult to determine the constants in the log law that best describe the overlap region mean velocity. Again, the diagnostic function is employed to give further insight into the logarithmic behaviour (see Fig. 11). The diagnostic function clearly shows the velocity profiles peeling up from the logarithmic law as Reynolds number increases, which is to be expected. At the lowest Reynolds number ($Re_\tau = 1770$), it is obvious that there is no substantial logarithmic region. However, even at the highest Reynolds number ($Re_\tau = 3880$), it could be argued that the wake region still begins as early as $z^+ = 100$. This supports the earlier conjecture that the logarithmic region is diminished by the adverse pressure gradient, such that there is almost no logarithmic behaviour evident.

The fact that the Reynolds number does not change the logarithmic region behaviour is an interesting result as it implies that the pressure gradient is responsible for the decrease in mean velocity below the log law. However, it is reminded that the Reynolds number range is still relatively small; further studies at higher Re_τ would be invaluable to better understand the scaling of adverse pressure gradient boundary layers.

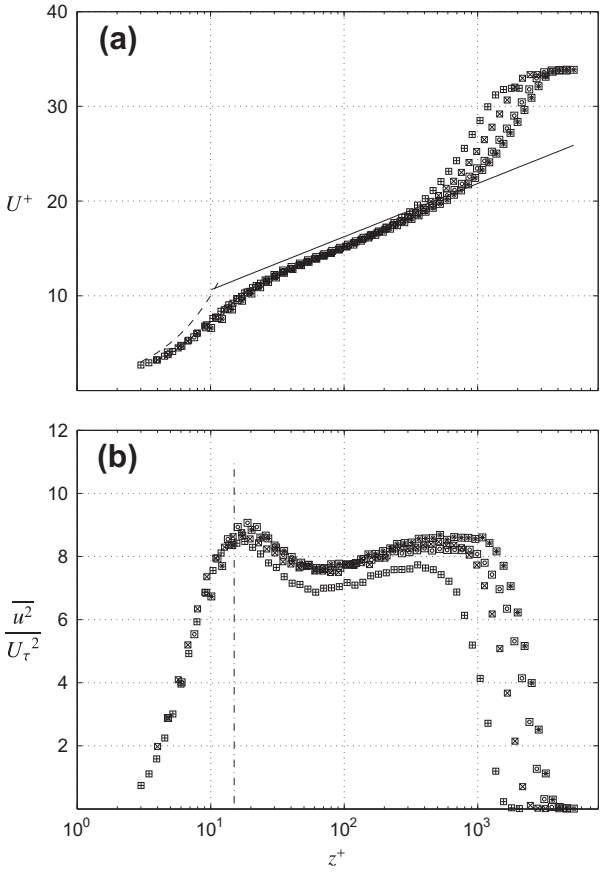

Fig. 10. APG flows at matched $\beta \approx 4.4$ in an increasing Re_τ (a) mean velocity profiles and (b) broadband turbulence intensity profiles. For symbols, refer to Table 2. Solid line shows $U^+ = \kappa^{-1}\log(z^+) + A$, $\kappa = 0.41$ and $A = 5.0$, dashed line shows $U^+ = y^+$ and dashed-dot line $z^+ = 15$.

Fig. 10*b* shows the broadband turbulence intensity profiles for $\beta \approx 4.4$. At $z^+ = 15$, the turbulence intensity maintains a similar magnitude (≈8.5–9) as Reynolds number increases. These values are obviously higher than those observed for zero pressure gradient data for similar Reynolds number (see Hutchins et al., 2009), owing to the increased large-scale energy caused by the pressure gradient. The higher Reynolds number data appear to collapse through most of the logarithmic region with the expected peel-off in the far outer region. This result suggests that there may be only slight differences in the structure of the flow with increasing Reynolds number in the near-wall and logarithmic regions at a constant pressure gradient. Although not shown here for brevity, the scale decomposition shows collapse of large- and small-scale contributions for all but the lowest Reynolds number. For the lowest Reynolds number, the large-scale contribution is lower in the outer region. This is not surprising since Hutchins and Marusic (2007) have shown that the large-scale contribution grows weakly logarithmically with Reynolds number.

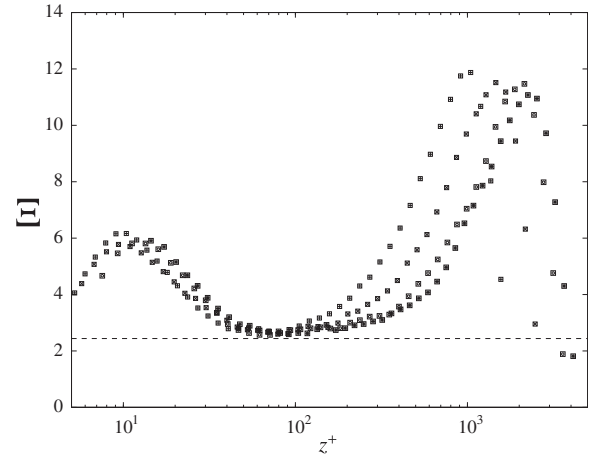

Fig. 11. The diagnostic function for APG flows at matched $\beta \approx 4.4$. For symbols, refer to Table 2. The dashed line shows $\kappa = 0.41$.

5.3. Constant acceleration parameter, K

As indicated in the introduction, there are a number of parameters that are used to quantify the pressure gradient. For comparison here we consider cases where the acceleration paramter K is held constant. Fig. 12*a* shows the mean velocity profiles for the experiments performed with matched $K \approx -1.5 \times 10^{-7}$. Note that both the pressure gradient and Reynolds number vary for each experiment ($0.96 < \beta < 4.75$ and $1910 < Re_\tau < 3630$). A systematic deviation below the classical log law is once again observed as β and Reynolds number increase. This implies that the deviation from the log law may be best described by a function of the pressure gradient parameter β only. At constant K, there is also an increase in the wake region with increasing β and Re_τ, which is expected.

Fig. 12*b* shows the broadband turbulence intensity profiles when K is constant. There is obviously no collapse of the

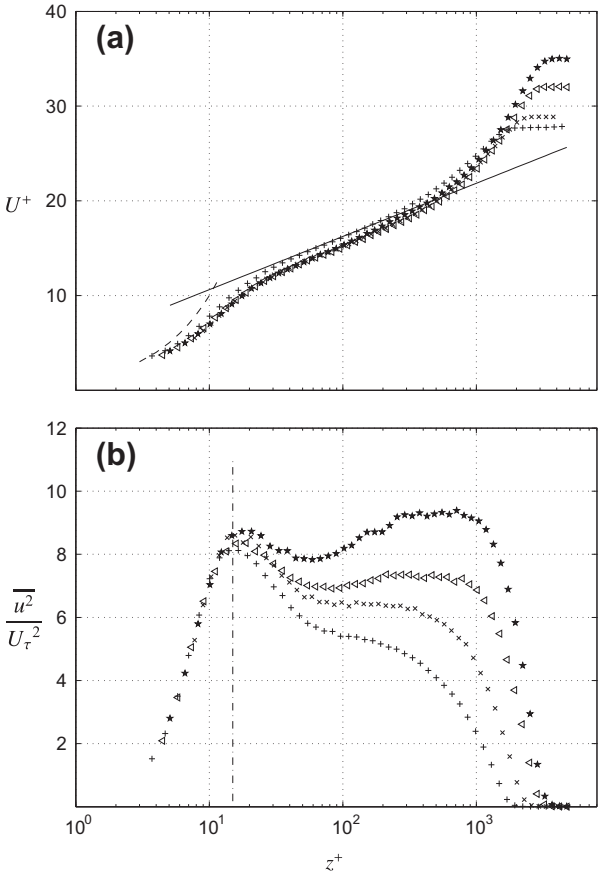

Fig. 12. APG flows at matched $K \approx -15.1 \times 10^{-8}$ (a) Mean velocity profiles and (b) broadband turbulence intensity profiles. For symbols, refer to Table 2. Solid line shows $U^+ = \kappa^{-1}\log(z^+) + A$, $\kappa = 0.41$ and $A = 5.0$, dashed line shows $U^+ = z^+$ and dashed-dot line $z^+ = 15$.

turbulence intensity with K in any region. As with the constant Re_τ data, an increase in turbulence intensity is observed as β and Re_τ increase, which is now known to be mainly due to the increased energy of the large-scale motions. The increasing turbulence intensity with matched K and the collapse of this statistic with constant β (see Section 5.1) suggests that it is β that is more useful for characterising the APG boundary layer.

6. Skewness and flatness

The skewness, S, and flatness, F, factors are defined as:

$$S = \frac{\overline{u'^3}}{(\overline{u'^2})^{3/2}}, \quad F = \frac{\overline{u'^4}}{(\overline{u'^2})^2}. \tag{6}$$

Fig. 13*a* shows the skewness of streamwise velocity fluctuations for varying pressure gradient. For the zero pressure gradient case, the skewness is negative in the lower part of the traditional logarithmic region $0.01 < z/\delta < 0.03$. Further from the wall ($0.03 < z/\delta < 0.15$), the pdf of streamwise velocity closely follows a Gaussian distribution (i.e., $S \approx 0$). These trends are consistent with previous findings (for example Balint et al. (1991)). Fig. 13*a* shows that the influence of the pressure gradient is to increase the skewness over the whole boundary layer, which was also reported by Nagano and Houra (2002). For the inner region, Nagano and Houra (2002) suggested that the rise in skewness is caused by 'structural changes in the near-wall' region due to pressure gradient. Here it is proposed that, for high Reynolds number ($Re_\tau \gtrsim 2000$), the change in skewness with pressure gradient is due to the increased large-scale influence in the near-wall region that was found earlier to be associated with increased β. A similar conjecture was made by Metzger and Klewicki (2001) who compared low Reynolds number laboratory data with that from a high Reynolds number atmospheric surface layer. At lower Reynolds number, it was found that in the inner region of $z^+ < 100$, the skewness was negative, while for the high Reynolds number data from the geophysical flow, the skewness remained positive in the same region. Upon applying a high-pass filter to the streamwise velocity component to separate low-frequency, large-scale motions, it was concluded that the increased energy of large-scale structures caused the increase in skewness from a negative to a positive value. It is therefore not surprising that the entire skewness profile increases with β, since it has already been shown that the large-scale energy over the entire boundary layer increases with pressure gradient.

Mathis et al. (2009) and Marusic et al. (2010b) have shown that the skewness is related to the amplitude modulation of the near-wall, small-scale structures by the large-scales. That study also reports the rise in skewness with Reynolds number for ZPG flows and show that this is explained by increased amplitude modulation. The behaviour of the skewness observed in Fig. 13*a* indicates that the large-scales are not only increasing in strength, but they are also increasingly amplitude modulating the small-scales as the pressure gradient increases.

Fig. 13*b* shows the flatness, F, of the streamwise velocity fluctuations for the constant Re_τ data. The zero pressure gradient flow has the lowest value of flatness in the near-wall region and, in general, the flatness increases with pressure gradient. In the outer region, the flatness is nearly invariant with pressure gradient. A rise in flatness is often attributed to a rise in intermittency (Dengel and Fernholz, 1990). This interpretation leads to the conclusion that there is weakly increasing intermittency in the near-wall region of the boundary layer as pressure gradient increases.

Fig. 14 shows the skewness and flatness of streamwise fluctuating velocity for constant pressure gradient parameter data with varying Re_τ. As with the lower-order statistics, the skewness

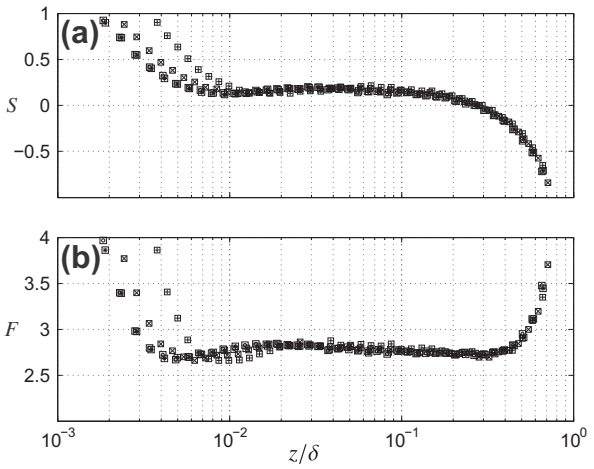

Fig. 14. (a) Skewness S and (b) flatness F for constant β 4.4 data. For symbols, refer to Table 2.

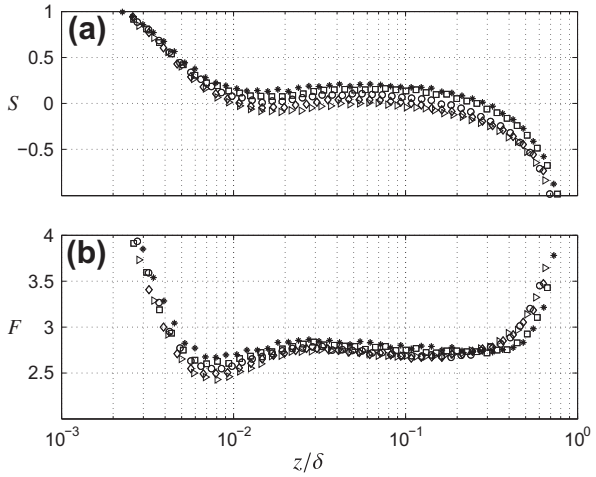

Fig. 13. (a) Skewness S and (b) flatness F for constant $Re_\tau \approx 1900$ data. For symbols, refer to Table 2.

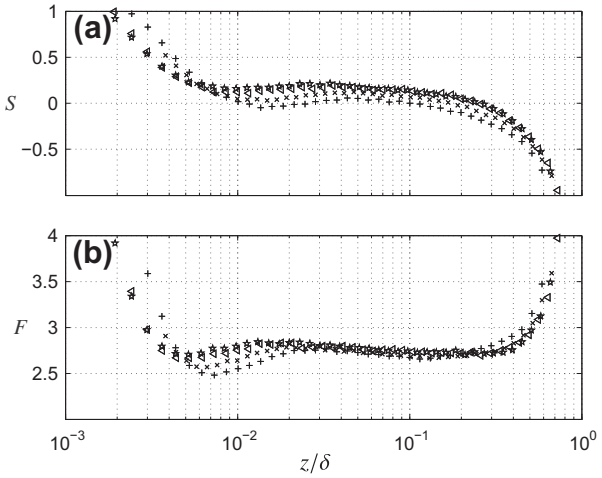

Fig. 15. (a) Skewness S and (b) flatness F for constant $K \approx -15.1 \times 10^{-8}$ data. For symbols, refer to Table 2.

collapses for all Reynolds numbers in the logarithmic and outer regions (the deviation near the wall is due to outer-scaling of the wall-normal coordinate, z). At this pressure gradient, the skewness remains positive through most of the layer, consistent with the data of Fig. 13. Similarly, flatness collapses for all of the constant pressure gradient data in the logarithmic and outer regions and, as with the skewness, a relatively constant deviation from a Gaussian distribution of velocity in the logarithmic and outer regions is observed.

For completeness, Fig. 15 displays the skewness and flatness of streamwise velocity fluctuations for the case of constant K. The trends are similar to Fig. 13: no collapse is observed in the skewness, which rises through most of the layer, and the flatness increases in the near wall region with increasing β.

7. Shape factor H

The behaviour of the shape factor, $H = \delta^*/\theta$, with increasing Reynolds number has recently been clarified by the work of Monkewitz et al. (2008) for zero pressure gradient flows. However, the pressure gradient (and upstream history) has a complex effect on the mean velocity and so the effect on the shape factor is not so well-understood (although it has been shown that the shape factor increases with β, see for example, Nagano et al., 1992; Spalart and Watmuff, 1993; Skåre and Krogstad, 1994). The additional complication is the dependence of H on Reynolds number, and, as discussed previously, many investigations allow both β and Re_τ to vary between experiments (as shown in the survey of existing data in Table 1). This makes it difficult to determine the behaviour of H, unless an impractically wide range of β and Re_τ is studied. In this investigation, each of the parameters has been isolated and this will hopefully provide some insight into the effect of pressure gradients on shape factor.

Monkewitz et al. (2008) developed a relationship between H and the Reynolds number based on displacement thickness, Re_{δ^*}; the shape factor continually decreases with increasing Re_{δ^*}. For this reason the shape factor is plotted against Re_{δ^*} in Fig. 16 for each of the experiments conducted. For the constant Re_τ experiments (note that Re_{δ^*} does not necessarily remain constant when Re_τ is kept constant if the pressure gradient is varied) the shape factor increases sharply as the pressure gradient increases. In contrast, the constant β data (symbols inside squares) decrease with increasing Reynolds number, as is the case for zero pressure gradient boundary layers.

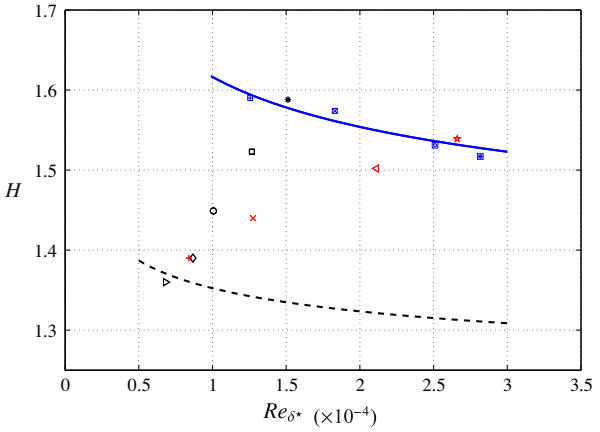

Fig. 16. Shape factor, H vs Re_{δ^*} for constant Re_τ, constant β data and constant K data. The dashed and the solid lines represent $H = (1 - I_{WW}/(\kappa^{-1}\log(Re_{\delta^*}) + C))^{-1}$ established by Monkewitz et al. (2008) with existing constants for ZPG and proposed constants for $\beta \approx 4.4$ shown in Table 3. For symbols, refer to Table 2.

Table 3
Summary of constants in Eq. (7) for ZPG and $\beta = 4.4$.

	(Monkewitz et al.) ZPG	$\beta \approx 4.4$
κ	0.384	0.36
C	3.3	2.3
I_{WW}	7.11	12.6

The formulation for the shape factor as a function of Re_{δ^*} determined by Monkewitz et al. can be written as

$$H = \left(1 - \frac{I_{WW}}{U_1^+}\right)^{-1} = \left(1 - \frac{I_{WW}}{\kappa^{-1}\log(Re_{\delta^*}) + C}\right)^{-1}, \quad (7)$$

where

$$I_{WW} = \int_0^\infty (U_1^+ - U^+)^2 d\eta.$$

Here $\eta = z/\Delta$ and $\Delta = \delta^* U_1^+$, C must be determined by curve-fitting (U_1^+, Re_{δ^*}) data. If the outer-scaled velocity defect profiles exhibit Reynolds number similarity, then I_{WW} is constant (it has been shown that $I_{WW} = 7.11$ in zero pressure gradient boundary layers). All three parameters for the ZPG case are provided in Table 3 and the resulting formulation is plotted as the broken line in Fig. 16. Since the constant β data appear to follow a similar trend, the parameters I_{WW}, κ and C were calculated for the $\beta \approx 4.4$ data. These are also presented in Table 3. It was possible to calculate $I_{WW} = 12.6$ from the velocity profiles because they exhibit Reynolds number similarity over the range studied (although not shown, velocity defect profiles collapse throughout the logarithmic and outer regions when β is held constant). It should be noted that, due to the limited data available (five Reynolds numbers), the values of the three parameters determined are estimates only. Nevertheless, the resulting formulation for H follows the data very well (the solid line in Fig. 16). Therefore, the evidence presented here suggests that the functional form of H with Reynolds number does not change with pressure gradient (at least not for mild pressure gradients and moderately high Reynolds numbers).

8. Conclusion

A parametric study in turbulent boundary layer flows subjected to adverse pressure gradients has been conducted. Specifically, three data sets were acquired with only one of the following parameters held constant in each set: pressure gradient parameter, β, Reynolds number or acceleration parameter, K.

The preceding discussion of results may be summarised as follows:

1. The oil-film interferometry method was used to determine the wall shear stress and it was shown that different results were obtained compared with the Clauser chart method for stronger pressure gradients ($\beta \gtrsim 2$).
2. In the traditionally accepted logarithmic region of the flow, there is a systematic decrease in mean velocity below the log law (fitted to the ZPG data) with increasing APG strength. Further inspection of this region revealed that the wake of the mean velocity profile in APG flows begins much closer to the wall than in the ZPG case. This leads to the conclusion that, for mild to strong adverse pressure gradients, there is effectively no identifiable logarithmic region (within the Reynolds number range of the study).
3. Reynolds number similarity is observed in the mean velocity profiles when β is held constant and the shape factor formulation of Monkewitz et al. (2008), developed for ZPG flows, appears to follow the data closely.

4. The large-scale structures in the turbulent boundary layer are clearly energised by the presence of the adverse pressure gradient. The increased energy of these large motions is felt throughout the layer and a higher broadband turbulence intensity results. Thus, the effect of pressure gradient on the turbulence intensity has similarities to the effect of increasing Reynolds number in zero pressure gradient flows. However, the amplification of the large-scale energy by the pressure gradient is much more severe than that due to Reynolds number for the experimental range reported in this investigation.
5. Skewness profiles show that increasing APG strength causes a rise in the skewness. Marusic et al. (2010b) have shown that increased skewness is a symptom of increased amplitude modulation of the small-scales of turbulence by the large-scales.

An extensive database of carefully acquired experimental results in APG boundary layers is presented here, which could be a valuable resource for numerical simulation validation and research into boundary layer control. However, there remain many open questions that will only be answered through further experimentation. The parametric approach adopted here has permitted a clearer insight into the importance of only a limited number of variables, leaving scope for similar studies considering other variables. This study has also been limited to the streamwise velocity component; experiments are planned to measure the other velocity components within a similar parameter space, but this remains a challenge due to the small size of the probes required to access the near-wall region. Perhaps of greatest need are APG data at higher Reynolds number, since investigations to date remain considerably distant in Reynolds number from those of important, high-energy-consuming engineering applications.

The authors are grateful for the support of the Australian Research Council.

References

Aubertine, C.D., Eaton, J.K., 2005. Turbulence development in a non-equilibrium turbulent boundary layer with mild adverse pressure gradient. J. Fluid Mech. 532, 345–364.

Balint, J.-L., Wallace, J.M., Vukoslavačević, P., 1991. The velocity and vorticity vector fields of a turbulent boundary layer. Part 2. Statistical properties. J. Fluid Mech. 228, 53–86.

Bourassa, C., Thomas, F.O., 2009. An experimental investigation of a highly accelerated turbulent boundary layer. J. Fluid Mech. 634, 359–404.

Chauhan, K., Ng, H.C.H., Marusic, I., 2010. Empirical mode decomposition and Hilbert transforms for analysis of oil-film interferograms. Meas. Sci. Technol. 21 (105405), 1–13.

Clauser, F.H., 1954. Turbulent boundary layers in adverse pressure gradients. J. Aero. Sci. 21, 91–108.

Coles, D., 1956. The law of the wake in the turbulent boundary layer. J. Fluid Mech. 1, 191–226.

Cutler, D.C., Johnston, J.P., 1989. The relaxation of a turbulent boundary layer in an adverse pressure gradient. J. Fluid Mech. 200, 367–387.

DeGraaff, D.E., Eaton, J.K., 2000. Reynolds-number scaling of the flat-plate turbulent boundary layer. J. Fluid Mech. 422, 319–346.

Dengel, P., Fernholz, H.H., 1990. An experimental investigation of an incompressible turbulent boundary layer in the vicinity of separation. J. Fluid Mech. 212, 615–636.

Ganapathisubramani, B., Longmire, E.K., Marusic, I., 2003. Characteristics of vortex packets in turbulent boundary layers. J. Fluid Mech. 478, 35–46.

Hutchins, N., Marusic, I., 2007. Large-scale influences in near-wall turbulence. Philos. Trans. Roy. Soc. A 365, 647–664.

Hutchins, N., Nickels, T.B., Marusic, I., Chong, M.S., 2009. Hot-wire spatial resolution issues in wall-bounded turbulence. J. Fluid Mech. 635, 103–136.

Jones, M.B., Marusic, I., Perry, A.E., 2001. Evolution and structure of sink-flow turbulent boundary layers. J. Fluid Mech. 428, 1–27.

Krogstad, P.-A., Skaȓe, P.E., 1995. Influence of a strong adverse pressure gradient on the turbulent structure in a boundary layer. Phys. Fluids 7, 2014–2024.

Lee, J.H., Sung, H.J., 2008. Effects of an adverse pressure gradient on a turbulent boundary layer. Intl. J. Heat Fluid Flow 29, 568–578.

Ligrani, P.M., Bradshaw, P., 1987. Spatial resolution and measurement of turbulence in the viscous sublayer using subminiature hot-wire probes. Exp. Fluids 5, 407–417.

Madad, R., Harun, Z., Chauhan, K., Monty, J., Marusic, I., 2010. Skin friction measurement in zero and adverse pressure gradient boundary layers using oil film interferometry. In: 17th Australasian Fluid Mechanics Conference, Auckland.

Marusic, I., Mathis, R., Hutchins, N., 2010a. High-Reynolds number effects in wall turbulence. Int. J. Heat Fluid Flow 31, 418–428.

Marusic, I., Mathis, R., Hutchins, N., 2010b. Predictive model for wall-bounded turbulent flow. Science 329 (5988), 193–196.

Marusic, I., McKeon, B.J., Monkewitz, P.A., Nagib, H.M., Smits, A.J., Sreenivasan, K.R., 2010c. Wall-bounded turbulent flows at high Reynolds numbers: recent advances and key issues. Phys. Fluids 22 (065103), 1–24.

Marusic, I., Perry, A.E., 1995. A wall-wake model for the turbulence structure of boundary layers. Part 2. Further experimental support. J. Fluid Mech. 298, 389–407.

Mathis, R., Hutchins, N., Marusic, I., 2009. Large-scale amplitude modulation of the small-scale structures in turbulent boundary layers. J. Fluid Mech. 628, 311–337.

Metzger, M., Klewicki, J., Bradshaw, K., Sadr, R., 2001. Scaling the near-wall axial turbulent stress in the zero pressure gradient boundary layer. Phys. Fluids 13 (6), 1819–1821.

Metzger, M.M., Klewicki, J.C., 2001. A comparative study of near-wall turbulence in high and low Reynolds number boundary layers. Phys. Fluids 13 (3), 692–701.

Monkewitz, P.A., Chauhan, K.A., Nagib, H.M., 2008. Comparison of mean flow similarity laws in zero pressure gradient turbulent boundary layers. Phys. Fluids 20 (10510), 1–16.

Monty, J.P., Stewart, J.A., Williams, R.C., Chong, M.S., 2007. Large-scale features in turbulent pipe and channel flows. J. Fluid Mech. 589, 147–156.

Nagano, Y., Houra, T., 2002. Higher-order moments and spectra of velocity fluctuations in adverse-pressure-gradient turbulent boundary layer. Exp. Fluids 33, 22–30.

Nagano, Y., Tagawa, M., Tsuji, T., 1992. Effects of adverse pressure gradients on mean flows and turbulence statistics in a boundary layer. Turbulent Shear Flows, Vol. 8. Springer, Berlin, pp. 7–21.

Nagano, Y., Tsuji, T., Houra, T., 1998. Structure of turbulent boundary layer subjected to adverse pressure gradient. Int. J. Heat Fluid Flow 19, 563–572.

Nagib, H.M., Chauhan, K.A., 2008. Variations of von Kármán coefficient in canonical flows. Phys. Fluids 20 (101518), 1–10.

Ng, H.C.H., Marusic, I., Monty, J.P., Hutchins, N., s. Chong, M., 2007. Oil film interferometry in high Reynolds number turbulent boundary layers. In: 16th Australasian Fluid Mechanics Conference, Gold Coast, pp. 807–814.

Nickels, T.B., 2004. Inner scaling for wall-bounded flows subject to large pressure gradients. J. Fluid Mech. 521, 217–239.

Österlund, J.M., Johansson, A.V., 2000. A note on the overlap region in turbulent boundary layers. Phys. Fluids 12, 1–4.

Perry, A.E., Marusic, I., Jones, M.B., 2002. On the streamwise evolution of turbulent boundary layers in arbitrary pressure gradients. J. Fluid Mech. 461, 61–91.

Samuel, A.E., Joubert, P.N., 1974. A boundary layer developing in an increasingly adverse pressure gradient. J. Fluid Mech. 66, 481–505.

Skote, M., Henningson, D.S., Henkes, R.A.W.M., 1998. Direct numerical simulation of self-similar turbulent boundary layers in adverse pressure gradients. Flow, Turbulence and Combustion 60, 47–85.

Skaȓe, P.E., Krogstad, P.-A., 1994. A turbulent equilibrium boundary layer near separation. J. Fluid Mech. 272, 319–348.

Smits, A.J., McKeon, B.J., Marusic, I., 2011. High-Reynolds number wall turbulence. Annu. Rev. Fluid Mech. 43, 353–375.

Spalart, P.R., 1986. Numerical study of sink-flow boundary layers. J. Fluid Mech. 172, 307–328.

Spalart, P.R., Watmuff, J.H., 1993. Experimental and numerical study of a turbulent boundary layer with pressure gradients. J. Fluid Mech. 249, 337–371.

Zagarola, M.V., Smits, A.J., 1998. Mean-flow scaling of turbulent pipe flow. J. Fluid Mech. 373, 33–79.